9. Because the probe antenna was not on the probe spin axis, spinning of the probe caused a similar, but smaller, effect.
10. By processing the VLA data in 0.1-s segments, the probe swinging is not resolved in the 10-Hz frequency bins. Processing the data in 1-s segments is possible and does show the probe swing in the received frequency. Longer segments were not used in the wind profile reported here due to processing time constraints.
11. The pressure of 0.4 bar occurs 20 km above the reference 1-bar level while 4 bar and 7 bar are 50 km and 75 km below the 1-bar level, respectively.
12. D. Atkinson, thesis, Washington State University (1989); J. B. Pollack, D. H. Atkinson, A. Seiff, J. Anderson, *Space Sci. Rev.* **60**, 143 (1992).
13. The design frequency of the probe USO-driven radio frequency was 1387.0 MHz. The frequency measured prior to launch was about 300 Hz higher than nominal with a drift that was not well determined. Our detected frequency was 465 ± 25 Hz higher than nominal.
14. F. H. Busse, *Astrophys. J.* **159**, 620 (1970); *Icarus* **29**, 255 (1976); P. J. Gierasch, *ibid.*, p. 445; A. P. Ingersoll and D. Pollard *ibid.* **52**, 62 (1982); K. Zhang and G. Schubert, *Science* **273**, 941 (1996).
15. Since a constant adjustment to our wind profile has been made based on the first few seconds of probe-orbiter data, the profile should agree with the profile based on the probe-orbiter data for those first few seconds given identical modeling. Part of the difference in derived wind speed at the initial time in Fig. 1 is due to characteristics of the polynomial fit applied to the probe-orbiter profile; a revision of the probe-orbiter profile (reduction in speed of about 20 m/s) due to better understanding of the orbiter Doppler receiver accounts for the remainder of the difference. Using a revised vertical descent profile, based on calibrated in situ probe temperature and temperature measurements, the Jupiter zonal wind speed profile based on only the probe-orbiter Doppler measurements has changed from (*7*) to agree better in character with Fig. 1 and indicates a lower average wind speed by about 20 m/s. D. Atkinson, private communication (1996).
16. L. A. Sromovsky *et al.*, *Science* **272**, 851 (1996); B. Ragent *et al.*, *ibid.*, p. 854.
17. G. Orton *et al.*, *ibid.*, p. 839.
18. We thank the following for their assistance in performing this experiment; D. Atkinson for helpful comments and probe-orbiter measurements; J. Ulvestad, E. M. Standish, D. Spitzmesser, and D. Jones of JPL; R. Perley, K. Sowenski, J. Wrobel, P. Dooley, M. Claussen, B. Butler, and the VLA staff; K. Wellington, M. Kesteven, R. Ferris, and the staff of the Australia Telescope; T. McElrath, F. Nicholson, and the rest of the Galileo navigation team; M. Smith, C. Sobeck, R. Sakal, P. Garriga, D. Carlock, and the rest of the Probe Project. The Very Large Array, part of the National Radio Astronomy Observatory, is operated by the Associated Universities, Inc., under cooperative agreement with the National Science Foundation. The Australia Telescope is funded by the Commonwealth of Australia for operation as a National Facility managed by CSIRO. The research described in this paper was, in part, carried out by the Jet Propulsion Laboratory, California Institute of Technology, under a contract with the National Aeronautics and Space Administration.

21 October 1996; accepted 30 December 1996

Microscopic Growth Mechanisms for Carbon Nanotubes

Jean-Christophe Charlier,* Alessandro De Vita, Xavier Blase,†
Roberto Car‡

The uncatalyzed edge growth of carbon nanotubes was investigated by first-principles molecular dynamics simulations. At experimental temperatures the open end of single-walled nanotubes closed spontaneously into a graphitic dome, which may explain why these nanotubes do not grow in the absence of transition metal catalysts. On the other hand, chemical bonding between the edges of adjacent coaxial tubes ("lip-lip" interactions) trapped the end of a double-walled nanotube in a metastable energy minimum, thus preventing dome closure. These calculations show that this end geometry exhibits a high degree of chemical activity and easily accommodates incoming carbon fragments, supporting a model of growth by chemisorption from the vapor phase.

Carbon nanotubes (*1*, *2*) are attracting much interest because of their potential applications in high-performing nanoscale materials (*3*, *4*) and electronic devices (*5*, *6*). Synthesis techniques for C nanotubes have recently achieved high production yields as well as good control of the tube geometry (*3*). Carbon nanotubes typically grow in an arc discharge at a temperature of ~3000 K. Transition metal catalysts are generally necessary to produce single-walled nanotubes (*7*) but are not required to produce multiwalled nanotubes, suggesting different growth mechanisms. However, the growth of C nanotubes cannot be directly observed, and the underlying microscopic mechanisms are still unclear (*3*).

The earliest models for growth of multiwalled C nanotubes (*8*, *9*) were based on topological considerations and emphasized the role of pentagonal and heptagonal rings capable of bending the straight hexagonal tubular network. The most debated issue was whether the ends of these nanotubes were open or closed during growth. In favor of the closed end mechanism, it was proposed that tubes grow by addition of atoms into the reactive pentagons present at the tip of the closed structure (*10*). However, recent experimental studies lend support to an open end growth mechanism (*11*, *12*), in which the atoms located at the open end of the graphitic structure provide active sites for the capture of C atoms from the plasma phase. Any capped configuration is more stable than the open end geometry, and therefore it was proposed that the latter could be stabilized by the high electric field present at the tip (*13*). However, recent first-principles calculations (*14*) have shown that this is not the case for realistic electric fields. Moreover, it is controversial whether in multiwalled nanotubes the inner or the outer tubes grow first (*9*, *15*) or whether different shells of the same tube may assist each other during growth (*16*, *17*). Finally, it is not clear why the growth of single-walled nanotubes, in contrast to that of the multiwalled nanotubes, generally requires the presence of metal catalysts (*7*, *12*).

In this work, we studied the microscopic mechanisms underlying the uncatalyzed growth of C nanotubes by performing first-principles molecular dynamics simulations of single- and double-walled nanotubes. In this approach (*18*) the forces acting on the atoms are derived from the instantaneous electronic ground state (*19*), which is accurately described within density functional theory in the local density approximation. We performed calculations on tubular nanotube sections terminated on one side by an open end and on the other side by H atoms that complete bonding to the two-coordinate C atoms (*20*). We considered a (10,0) "zigzag" nanotube (Fig. 1A), a (5,5) "armchair" single-walled nanotube, and a (10,0)@(18,0) "zigzag" double-walled nanotube (Fig. 2A) (*21*).

During the course of the simulation, the open end of the (10,0) single-walled tube closed into a structure with no residual two-coordinate atoms (Fig. 1, A through C). This closed structure is more stable than the initial open end structure by ~18 eV (that is, ~1.8 eV per initial two-coordinate C atom). This is still 4.6 eV less stable than the "ideal" C_{60}-hemisphere cap, which contains only hexagons and isolated pentagons. However, the time scale of our simulation prevented us from studying the further evolution of the tip geometry.

A similar calculation for the (5,5) single-walled nanotube led to tip closure into a hemi-C_{60} with an energy lowering of ~15 eV. In this case the open nanotube edge consists of dimers, rather than single atoms

---

Institut Romand de Recherche Numérique en Physique des Matériaux, Ecublens, CH-1015 Lausanne, Switzerland.

*Permanent address: Unité de Physico-Chimie et de Physique des Matériaux, Université Catholique de Louvain, Place Croix du Sud 1, B-1348 Louvain-la-Neuve, Belgium.

†Permanent address: Département de Physique des Matériaux (UA 172), Université Claude Bernard, 43 bd. du 11 Novembre 1918, F-69622 Villeurbanne Cedex, France.

‡To whom correspondence should be addressed.

as in Fig. 1A, and therefore its chemical reactivity is lower. This is presumably the reason why we observed the first pentagonal rearrangement only after 1.0 ps of simulation at ~3000 K. We expect that similar self-closing processes would also occur in simulations of other single-walled nanotubes with a diameter in the experimental range of 0.8 to 2.0 nm (*7*, *12*). The observation that the open ends of single-walled nanotubes reconstructed and closed so easily during the short time span of our simulation may explain why, during synthesis, open end single-walled nanotubes cannot exist in a pure C environment.

We find that tip closure results in a substantial reduction in the localized density of electron states (LDOS) on the tips close to the Fermi energy. This result suggests that the reactivity of closed nanotube tips for any realistic bond topology of the cap should be considerably lower than that of open end nanotubes. Therefore, it is unlikely that during typical synthesis conditions single-walled nanotubes could grow by sustained incorporation of C atoms into the closed tip. This is in agreement with

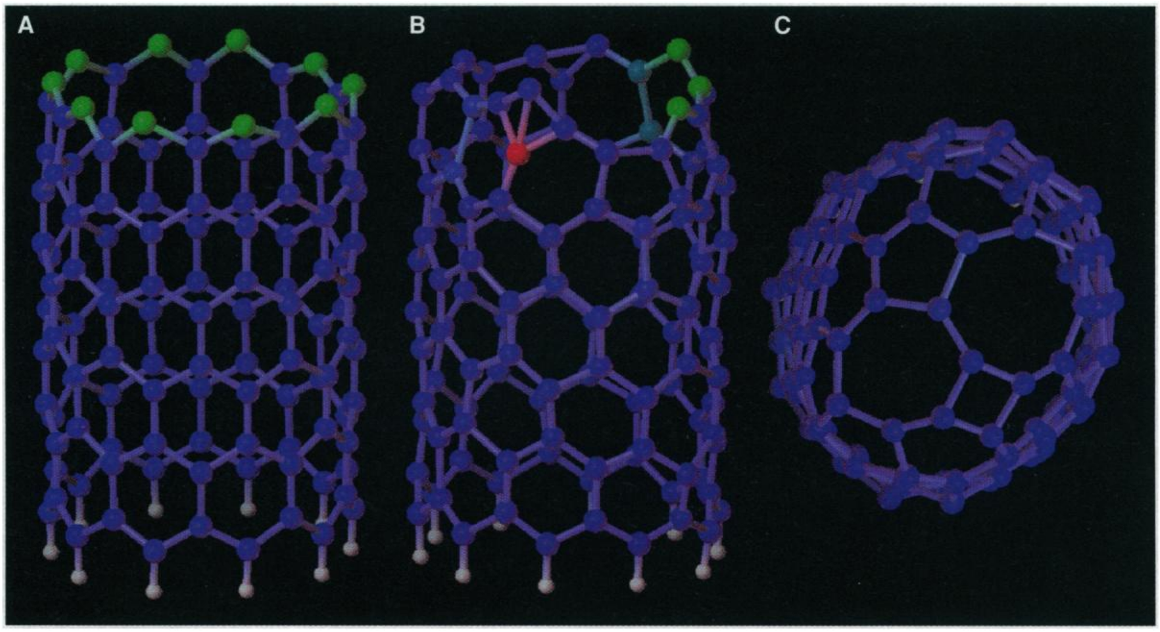

Fig. 1. Spontaneous closure of a (10,0) single-walled C nanotube. The diameter of this tube (0.8 nm) is consistent with a dominant peak observed in the diameter frequency histogram of synthesized single-walled nanotubes (*7*). The model contains 120 C atoms (large violet, green, or red spheres) and 10 H atoms (small white spheres). Red, violet, and green spheres represent coordination of 4, 3, and ≤2, respectively. Coordinations between 2 (green) and 3 (violet) are represented by the intermediate color palette. The H atoms and the neighboring bottom ring of C atoms were kept fixed during the simulation. (**A**) Side view of the open-end starting configuration at 0 K, with 10 two-coordinate C atoms at the top edge. (**B**) At ~1500 K, the first pentagon is created from one of the top hexagonal rings, resulting in substantial inward bending. The extra C atom moves aside, forming two edge-sharing three-membered rings. The formation of two more pentagons by the same mechanism was observed at temperatures below 2500 K. (**C**) Top view of the close-ended configuration, after 5 ps at 3500 K. The nanotube is fully reconstructed with no residual two-coordinate atoms left. The final cap topology is composed of seven hexagons, five pentagons, one heptagon, one octagon, and two squares, consistent with Euler's theorem (*3*).

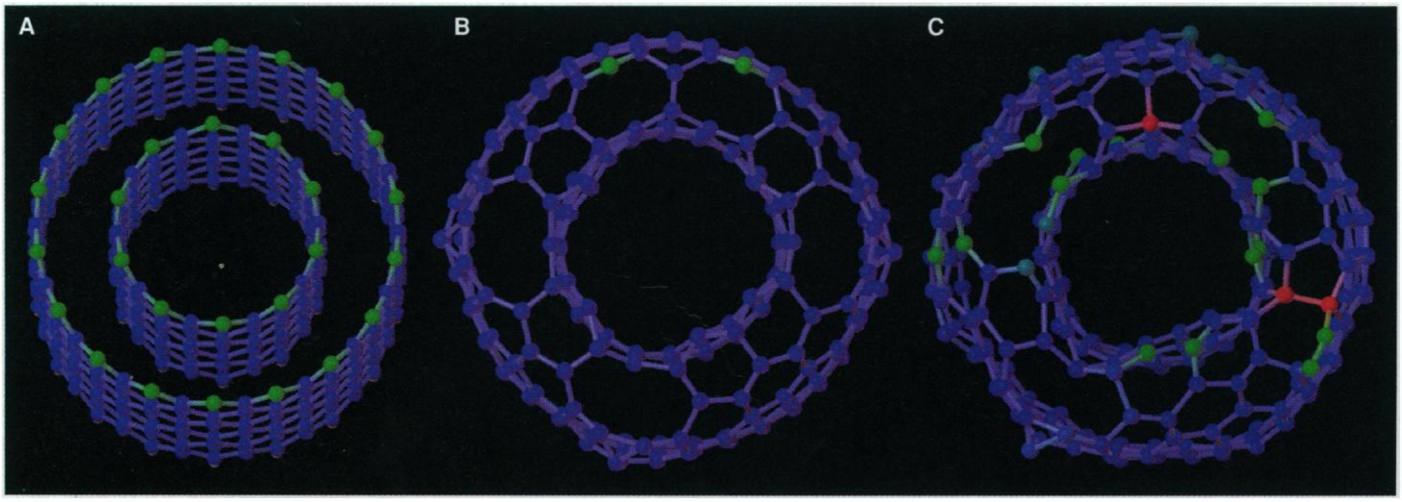

Fig. 2. Stabilization of a (10,0)@(18,0) double-walled C nanotube edge by "lip-lip" interactions. The interlayer distance is 3.3 Å, in good agreement with experimental results (*2*). The model contains 336 C and 28 H atoms. The color scheme is as defined in the legend to Fig. 1. (**A**) Top view of the open-end starting bilayer system at 0 K, with 28 two-coordinate C atoms at the top edge. (**B**) Top view of the lip-lip interacting concentric shells at ~300 K. The topmost atoms of the adjacent tube shells moved rapidly toward each other, forming 10 bridging bonds. The presence of two remaining two-coordinate atoms is favored by the incommensurability of the graphene networks. (**C**) Snapshot of the same system after 2.8 ps of simulation at ~3000 K, illustrating the fluctuating lip-lip bond network. At this temperature, the bond topology of the edge strongly fluctuated, and a time span of ~100 fs was sufficient to produce a different edge configuration, albeit with the same overall characteristics.

simulations showing that C atoms are not incorporated into C_{60} (*22*).

In the case of the (10,0)@(18,0) multiwalled nanotube, we found that the open end bilayer structure was trapped into a metastable energy minimum by the formation of bridging bonds between the edges of the adjacent tubes (Fig. 2, A through C). This "lip-lip" interaction mechanism, first suggested in (*23*), inhibited the dome closure observed for the single-walled tubes. The energy lowering due to lip-lip interactions is $\sim$1 eV per initial two-coordinate C atom.

During 1.5 ps of simulation at $\sim$3000 K, we observed only one isolated exchange between atoms at the tube edge, suggesting low diffusional barriers. However, at $\sim$3000 K, the bridging bonds connecting the inner and the outer tubes continuously broke and re-formed on the time scale of the C–C bond-stretching modes (Fig. 2C). This "fluctuating lip-lip bond" character of the edge structure indicates the existence of several equivalent metastable configurations of the bridging bonds, separated by small energy barriers. All these edge structures display a large LDOS at the Fermi level, yielding a high chemical reactivity. This is a consequence of the large curvature (roughly twice that of C_{60}) of the bridging bond region, which is known to induce metallization by σ^*-π^* hybridization (*24*). The LDOS at the Fermi level is further enhanced by the presence of low-coordinate C atoms (Fig. 2C).

The fluctuating lip-lip bonds should provide active sites for absorption. To investigate this possibility, we studied the impact of C fragments on the tube edge at $\sim$3000 K. In our simulations, the impinging fragments initially moved parallel to the nanotube axis with thermal velocity, starting at $\sim$3 Å from the edge. In one case, we considered two isolated C atoms simultaneously approaching the edge. In order to sample different impact scenarios, one of the atoms was projected toward a two-coordinate atom and the other toward the middle of a hexagonal ring (Fig. 3, A and B). Both atoms were incorporated into the fluctuating network of the nanotube edge, so that, within less than 0.5 ps of simulation, they could no longer be distinguished from the atoms of the original nanotube. In another simulation, we projected a C dimer onto a region of bridging bonds, choosing a parallel impact geometry (*25*), and in this case also we observed fast incorporation by the tube edge.

The above results suggest a possible growth mechanism in which incorporation of C atoms from the vapor phase is mediated by the fluctuating lip-lip bonds of the tube edge. This mechanism is reminiscent of the vapor-liquid-solid (VLS) model introduced in the 1960s to explain the growth of silicon whiskers (*26*). In this model, growth occurs by precipitation from a supersaturated liquid-metal-alloy droplet located at the top of the whisker, into which silicon atoms are preferentially absorbed from the vapor phase. The similarity between the growth of C nanotubes and the VLS model has also been pointed out by Saito *et al.* on the basis of their experimental findings for multiwalled nanotube growth in a purely C environment (*16*). Solid C sublimates before it melts at ambient pressure, and therefore these investigators suggested that some other disordered C form with high fluidity, possibly induced by ion irradiation, should replace the liquid droplet. In the microscopic model provided by our simulation, it is not so much the fluid nature of the edge but the fluctuating character of the lip-lip bonds that makes possible a rapid incorporation of C fragments.

Our results for single-walled nanotubes should be contrasted with those obtained for double-walled nanotubes. In the former case dome closure makes uncatalyzed growth unfavorable, whereas in the latter the existence of a metastable edge structure may explain why multiwalled nanotubes can grow by a noncatalytic process. The minimal growing unit required for the lip-lip interaction is a tube pair. A multiple dome closure of two or three (and sometimes more) tube shells at the interior of a multiwalled nanotube has been observed experimentally (*8*, *27*), suggesting a correlated shell-growth mechanism.

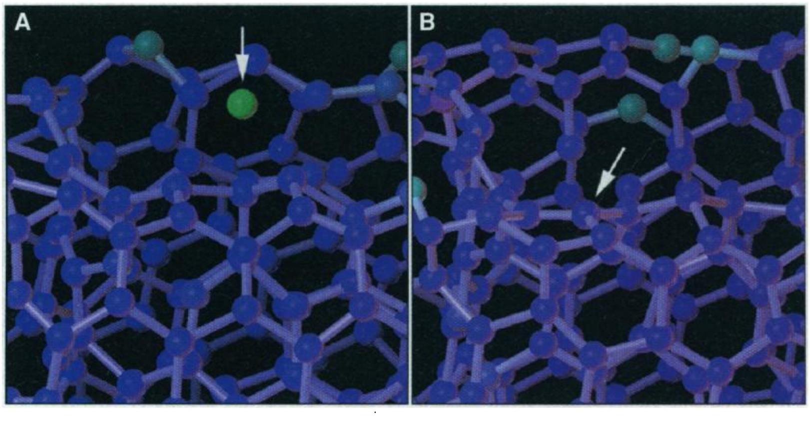

Fig. 3. Schematic showing the result of the incorporation of an extra C atom into a tube edge at $\sim$3000 K. The color scheme is as defined in the legend to Fig. 1. (**A**) The extra atom (white arrow) is approaching a hexagonal ring of the edge with an initial kinetic energy of 0.125 eV. (**B**) After incorporation, the extra atom has become three-coordinated. The time elapsed since (A) is $\sim$0.2 ps.

REFERENCES AND NOTES

1. S. Iijima, *Nature* **354**, 56 (1991).
2. T. W. Ebbesen and P. M. Ajayan, *ibid.* **358**, 220 (1992).
3. T. W. Ebbesen, *Phys. Today* **49**, 26 (1996).
4. M. M. J. Treacy, T. W. Ebbesen, J. M. Gibson, *Nature* **381**, 678 (1996).
5. W. A. de Heer, A. Châtelain, D. Ugarte, *Science* **270**, 1179 (1995).
6. R. F. Service, *ibid.* **271**, 1232 (1996); R. Saito, G. Dresselhaus, M. S. Dresselhaus, *Phys. Rev. B* **53**, 2044 (1996); J.-C. Charlier, T. W. Ebbesen, Ph. Lambin, *ibid.*, p. 11108; L. Chico *et al.*, *Phys. Rev. Lett.* **76**, 971 (1996).
7. S. Iijima and T. Ichihashi, *Nature* **363**, 603 (1993); D. S. Bethune *et al.*, *ibid.*, p. 605.
8. S. Iijima, T. Ichihashi, Y. Ando, *ibid.* **356**, 776 (1992).
9. S. Iijima, *Mater. Sci. Eng. B* **19**, 172 (1993).
10. M. Endo and H. W. Kroto, *J. Phys. Chem.* **96**, 6941 (1992); R. Saito, G. Dresselhaus, M. S. Dresselhaus, *Chem. Phys. Lett.* **195**, 537 (1992).
11. S. Iijima, P. M. Ajayan, T. Ichihashi, *Phys. Rev. Lett.* **69**, 3100 (1992).
12. C.-H. Kiang and W. A. Goddard III, *ibid.* **76**, 2515 (1996); A. Thess *et al.*, *Science* **273**, 483 (1996).
13. R. E. Smalley, *Mater. Sci. Eng. B* **19**, 1 (1993).
14. A. Maiti, C. J. Brabec, C. M. Roland, J. Bernholc, *Phys. Rev. Lett.* **73**, 2468 (1994); L. Lou, P. Nordlander, R. E. Smalley, *Phys. Rev. B* **52**, 1429 (1995).
15. X. F. Zhang *et al.*, *J. Crystal Growth* **130**, 368 (1993).
16. Y. Saito *et al.*, *Chem. Phys. Lett.* **204**, 277 (1993).
17. E. G. Gamaly and T. W. Ebbesen, *Phys. Rev. B* **52**, 2083 (1995).
18. R. Car and M. Parrinello, *Phys. Rev. Lett.* **55**, 2471 (1985).
19. By keeping the electrons in the ground state, we neglect the thermal broadening of the energy distribution of the occupied electron states. However, even at $\sim$3000 K, this broadening is small compared to the occupied band width and is not expected to significantly affect the results of the simulations.
20. We described the interaction between valence electrons and ionic cores by using norm-conserving pseudopotentials for C [N. Troullier and J. L. Martins, *Phys. Rev. B* **43**, 1993 (1991)] and for H [G. B. Bachelet, D. R. Hamann, M. Schlüter, *ibid.* **26**, 4199 (1982)]. We adopted periodic boundary conditions, keeping a minimum 5 Å distance between repeated images. This condition is sufficient to ensure negligible interaction between the images. The electronic wave functions at the Γ-point of the supercell Brillouin zone and the electron density were expanded into plane waves with kinetic energy cutoffs of 40 and 120 rydbergs, respectively. The calculated intraplanar lattice constant of graphite, 2.46 Å, and the C–C bond lengths in C_{60}, 1.40 Å and 1.47 Å, agree with the experimental results to within 1%.
21. We adopted the notation of N. Hamada, S.-I. Sawada, and A. Oshiyama [*Phys. Rev. Lett.* **68**, 1579 (1992)]. All nanotubes were initially relaxed to their open end equilibrium geometries before being gradually heated to temperatures of $\sim$3000 to 3500 K by means of a Nosé thermostat (*28*). Typical rates for temperature variation were between 250 and

1500 K/ps. We performed the simulations on a massively parallel computer (*29*), using a time step of 0.7 fs, for a total time of ~30 ps.

22. B. R. Eggen *et al.*, *Science* **272**, 87 (1996).
23. T. Guo *et al.*, *J. Phys. Chem.* **99**, 10694 (1995).
24. X. Blase, L. X. Benedict, E. L. Shirley, S. G. Louie, *Phys. Rev. Lett.* **72**, 1878 (1994); J.-C. Charlier, Ph. Lambin, T. W. Ebbesen, *Phys. Rev. B* **54**, R8377 (1996).
25. The molecular axis was initially orthogonal to the nanotube axis and oriented along a line not including the latter.
26. R. S. Wagner and W. C. Ellis, *Appl. Phys. Lett.* **4**, 89 (1964).
27. S. Seraphin, D. Zhou, J. Jiao, *Microscop. Acta* **3**, 64 (1994).
28. S. Nosé, *Prog. Theor. Phys. Suppl.* **103**, 1 (1991).
29. A. De Vita, A. Canning, R. Car, *EPFL Supercomput. J.* **6**, 22 (1994).
30. Supported in part through the Parallel Application Technology Program between the École Polytechnique Fédérale de Lausanne (EPFL) and Cray Research, and by the Swiss NSF (grant 20-39528.93).

J.-C.C. was supported by the National Fund for Scientific Research of Belgium and by a Human Capital and Mobility Grant of the European Union. X.B. was funded in part by the Communauté de Travail des Alpes Occidentales (CO-TRAO). We are grateful to M. Teschner for providing the graphics tools used in the work and to A. Canning for his contribution to the development of the parallel code.

29 August 1996; accepted 6 December 1996

A Silicon Single-Electron Transistor Memory Operating at Room Temperature

Lingjie Guo, Effendi Leobandung, Stephen Y. Chou*

A single-electron memory, in which a bit of information is stored by one electron, is demonstrated at room temperature. The memory is a floating gate metal-oxide-semiconductor transistor in silicon with a channel width (~10 nanometers) smaller than the Debye screening length of a single electron and a nanoscale polysilicon dot (~7 nanometers by 7 nanometers) as the floating gate embedded between the channel and the control gate. Storing one electron on the floating gate screens the entire channel from the potential on the control gate and leads to (i) a discrete shift in the threshold voltage, (ii) a staircase relation between the charging voltage and the shift, and (iii) a self-limiting charging process. The structure and fabrication of the memory should be compatible with future ultralarge-scale integrated circuits.

To increase the storage density of semiconductor memories, the size of each memory cell must be reduced. A smaller memory cell also leads to faster speeds and lower power consumption. One of the widely used nonvolatile semiconductor memories is the metal-oxide-semiconductor (MOS) transistor that has a floating gate between the channel and the control gate. Information is represented by storing charges on the floating gate. The information can be read by using the transistor because different amounts of charge on the floating gate shift the threshold voltage of the transistor differently. The ultimate limit in scaling down the floating gate memory is to use one electron to represent a bit, the so-called single electron MOS memory (SEMM). To make such memory practical requires a proper design of device structure, so that the voltage for charging a single electron is discrete and well separated (as compared to the noise level), as is the shift in threshold voltage caused by the storage of a single electron.

One of the two previous approaches to SEMM is to build the device in a tiny polysilicon strip (*1*). An electron percolation path in the strip forms the channel, and one of polysilicon grains near the conduction path acts as the floating gate. Such a structure intrinsically prevents precise control of the channel size, floating gate dimension, and tunnel barrier. The other approach is to replace the floating gate of conventional floating gate transistor memory with nanocrystal grains, while keeping the rest of the device unaltered (*2*). The size of the silicon nanocrystals and the tunnel barriers intrinsically have a broad distribution. Both approaches intend to alleviate the challenges in nanofabrication, but the statistical variations in their structures lead to large fluctuations in the shift of the threshold voltage and in the charging voltage, making them unsuitable for large-scale integration.

Here we present a SEMM in crystalline silicon that has a well-controlled dimension. Charging a single electron to the floating gate leads, at room temperature, to a quantized shift in threshold voltage and a staircase relation between the shift and the charging voltage. Furthermore, the charging process is self-limited.

There are two key features of our SEMM (Fig. 1): (i) the channel width of silicon MOS field-effect transistor is narrower than the Debye screening length of a single electron and (ii) the floating gate is a nanoscale square (hence, it is called a dot) (*3*). Otherwise, the device is similar to an ordinary floating gate MOS memory. The narrow channel ensures that the storage of a single electron on the floating gate is sufficient to screen the entire channel (that is, the full channel width) from the potential on the control gate, which leads to a significant shift in threshold voltage. A small floating gate is used to significantly increase electron quantum energy (due to the small size) and electron charging energy (due to the small capacitance); hence, the threshold voltage shift and the charging voltage become discrete and well separated at room temperature. The control gate in our device is long, but the device's threshold is determined by the section where the floating gate is located.

In fabrication, an 11-nm-thick polysilicon film (for the floating gate) was deposited on a silicon-on-insulator wafer that had a 35-nm-thick top layer of crystalline silicon (for the channel). The polysilicon film and the silicon layer were separated by a layer of native oxide ~1 nm thick. The first level of electron beam lithography (EBL) and reactive ion etching (RIE) patterned the width of the floating gate and the narrow silicon channel, which is under the gate (that is, they are self-aligned). The initial channel width varied from 25 to 120 nm. A second level of EBL and RIE patterned the length of the floating gate, making it square (Fig. 2). An 18-nm-thick layer of oxide was then thermally grown, partially consuming the silicon, which reduced the thickness of the polysilicon dot by ~9 nm and the lateral size of the dot and the width of the silicon channel by ~18 nm. A 22-nm-thick layer of oxide was deposited by plasma-enhanced chemical vapor deposition, making the total thickness of the control gate oxide 40 nm. Next, polysilicon was deposited, and the control gate was patterned to a length of 3 μm, which covered the floating gate and part of the narrow channel.

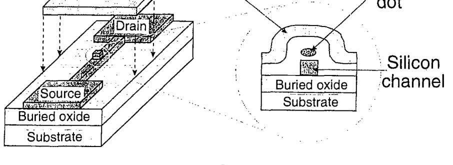

Fig. 1. Schematic of a SEMM that has a narrow silicon channel and a nanoscale polysilicon dot as the floating gate. The cross-sectional view details the floating gate and the channel region.

Nanostructure Laboratory, Department of Electrical Engineering, University of Minnesota, Minneapolis, MN 55455, USA.

*To whom correspondence should be addressed. E-mail: chou@ee.umn.edu